

Elemental doping and size effects modified **biomass-derived carbon**: a fascinating microwave absorbing/shielding and energy saving material

Ali Fahimi ^{a,b,c}; Pouyan Fakharian ^{d,e}; Ali Mirakhan ^{b,c}; Atiye Farahani ^f; Zehua Zhou ^{g*}; Yue Zhao ^g; Reza Peymanfar ^{h,b,c,*}

^a Department of Construction Engineering and Management, Energy Institute of Higher Education, Saveh P.O. Box 39177-67746, Iran

^b Iranian Society of Philosophers, Department of Science, Tehran, Iran

^c Sustainable Development of Industrial Laboratory (SDILAB) CO., Tehran, Iran

^d Institute of Research and Development, Duy Tan University, Da Nang, Vietnam

^e School of Engineering & Technology, Duy Tan University, Da Nang, Vietnam

^f Department of Civil Engineering, Tafresh University, Tafresh P.O. Box 39518-79611, Iran

^g College of Materials Science and Technology, Nanjing University of Aeronautics and Astronautics, Nanjing 210016, People's Republic of China

^h Department of Chemical Engineering, Energy Institute of Higher Education, , Saveh P.O. Box 39177-67746, Iran

Ali Fahimi

ali9386687@gmail.com

<https://orcid.org/0000-0001-9850-1118>

Pouyan Fakharian

pouyanfakharian@duytan.edu.vn

<https://orcid.org/0000-0003-4307-1944>

Ali Mirakhan

ali.mirkhan@peykareh.com

<https://www.scopus.com/authid/detail.uri?authorId=57681654600>

AtiyeFarahani

afarahani@tafreshu.ac.ir

<https://orcid.org/0000-0003-1658-7021>

Yue Zhao

nuaazhaoy@163.com

<https://www.scopus.com/authid/detail.uri?authorId=56997852800>

* Corresponding authors:

Reza Peymanfar

reza_peymanfar@alumni.iust.ac.ir
<https://orcid.org/0000-0001-9850-1118>

Zehua Zhou
17852831781@163.com

Abstract

The center of polarization induced by hybrid elements and the size effect are proved to be effective ways to enhance microwave absorption. The effects of specific surface area ratio and doping of elements (P, S, N) on microwave absorption characteristics were studied with almond shell as raw material, and the particle size effect was evaluated by ball milling scenario. The modified material obtained a doped conjugated porous structure, and red phosphorus implanted carbon nanotubes onto the bio-based surface. It is interesting to note that cement is used as the absorbing substrate to make the absorbing composite material and show fascinating electromagnetic interference shielding effect (EMI SE) and microwave absorption properties. For example, S-BPAS with a thickness of 3.15 mm obtained a reflection loss (RL) of 99.42 dB, while BPAS with an ultra-low thickness of 1.20 mm obtained a wide effective bandwidth of 5.38 GHz. In particular, the total SE of BPAS and P-BPAS in the x and ku bands is $\geq 90\%$. The research results open up a new prospect for the development of advanced functional materials that can save energy and purify electromagnetic pollution.

Keywords: Microwave absorption, Electromagnetic interference shielding effectiveness (EMI SE), Building material, Biomass-derived materials, Energy-saving structures

1. Introduction

With the advent of carbon nanotube (CNT) by Iijima, novel prospects have emerged for developing nanotechnology ¹. Various applications were promoted, benefiting from the vast surface area to volume ratio of the conjugated carbon-based material with unique morphologies. The special mechanical feature, electric and thermal conductivity, hydrophobicity, physiochemical and thermal stability, and processability, besides the aforementioned properties, lead to widespread knowledge-based technologies in: (1) Energy, including thermoelectric, triboelectric, photovoltaic, phase change materials (PCM), supercapacitors, batteries, heat transfer, IR absorber/reflector, and catalysts, (2) polymer, comprising strengthening mechanical properties of the conventional polymers, biomedical application, (3) material science, consisting of corrosion engineering and alloy manufacturing, (4) environment such as refining electromagnetic pollution and filters, and other fields like military technology, medicine, pharmacology, and so on ²⁻⁷. Diverse efforts have been made to tailor single-walled carbon nanotubes (SWCNTs) and multiple-walled carbon nanotubes (MWCNTs) as well as tune chirality, length, and diameter using chemical vapor deposition

(CVD) and arc discharge ^{8, 9}. The special electric/thermal conductivity and broad conjugate surface area bringing superior polarization loss and manipulable surface area cause to selection of CNTs as pioneer candidates for electromagnetic refining and energy-saving material.

It is well known that climate change and electromagnetic pollution in the modern century, like a volcano waiting to erupt, have augmented the global burden ¹⁰⁻¹⁹. The proposed research has presented two distinct and complementary approaches, simultaneously exploring how to refine the electromagnetic pollution and save energy consumption by tailoring a building material. A microwave-absorbing material with intense and broadband performance as well as affordable, processable, lightweight, simple, and catchable structure has been a mermaid, investigated by scientists. Biomass-derived structures were widely used to fabricate microwave-absorbing materials rooted in their conductive, affordable, lightweight, sustainable, and polarizable nature ²⁰. Particularly, the Debye-relaxation theory and recent literature provide evidence that size and morphology pave the way for microwave attenuation ^{21, 22}. Defect, size, morphology, and doping as essential factors to modify the dipole and interfacial polarization, conductivity, impedance matching, quasi-antenna, and metamaterial characteristics play a significant role in adjusting the microwave absorption capacity ²³⁻³⁴. Energy consumption will ever-increasingly burgeon more than fourfold in the United

States over the next 20 years, derived from climate change and population growth. Thus, energy-saving is under the spotlight. Heat transition is based on conduction, convection, and radiation. The obtained heat (about 50%) during a day is placed in IR wavelength, warming the earth. Hence, IR absorption/reflection plays a pivotal role in energy-saving field. Accordingly, the presented approach was considered in the design of building materials and ameliorating the building sustainability using diverse structures such as transparent wood and hydrogel, wood, polystyrene, polymethyl methacrylate, slag wool, polydimethylsiloxane, paint, glass, polyurethane, rock, cellulose, epoxy, cotton, polyvinyl butyral, brick, ceramic products, pulp, cane, polyethylene, etc.³⁵⁻⁴⁰.

To tackle the above-mentioned problems, in this study, almond shell was applied as a biomass source, demonstrating fabulous microwave absorbing characteristics after pyrolysis, originating from its broad specific surface area of the conjugated structure. More interestingly, the influence of the size and specific surface area of the bio-inspired structure was assessed by aiding a facile ball-milling process, improving the microwave-absorbing mechanisms. More importantly, an innovative approach was presented for doping the bio-waste using novel precursors and experimental procedures. N, P, and S elements anchored into the conductive carbonaceous structure after the pyrolysis scenario to strengthen the dipole polarization and impedance matching. Interestingly, P implanted CNTs onto the

bio-waste for the first time in the world by solvothermal method using red phosphorous as a catalyst. Eventually, cement as a building material and microwave-absorbing medium was employed to boost practical applications of this knowledge-based product. The IR and microwave-absorbing features of the cement-based structures were scrupulously dissected.

2. Experimental

2. 1. Materials

The energy-saving and microwave-absorbing structures were prepared by melamine (99.0 %) and N-Methyl-2-pyrrolidone (NMP, 99.5 %) supplied by Sigma-Aldrich) as well as phosphorus (red, ≥ 97.0 %), sulfur (99.0 - 101.0 %), glycerol (≥ 99.5 %), ethanol (≥ 99.5 %), cyclohexane (≥ 99.5 %) purchased from Merck without further purification. Notably, the inorganic matrix was fabricated by type 2 Portland cement obtained from Saveh Cement Co.

2. 2. Fabrication of biomass-derived materials

Almond shells were received from a local area in Saveh-Iran (Yolagh). To evaluate the size influence on the microwave-absorbing and energy-saving characteristics, the almond shells were initially rinsed several times with deionized water and ethanol by aiding ultrasonic waves. Then, the dried shells were grinded in mortar for 5 min or ball milled for 5 min at a frequency of 30 Hz. Next, the obtained structures were pyrolyzed at 850 °C for 3 h. The doping effect on the microwave-

absorbing and energy-saving features was explored by doping S, N, and P elements. Sulfur, red phosphorous, and melamine were used as the source of the dopants. To tackle the purpose, the precursors were respectively dissolved in cyclohexane, NMP, and glycerol as solvents. The same paradigm in mass fraction between the dopants and pyrolyzed structures was elected equaling 5 wt %. Afterward, the suspensions were treated by a Teflon-lined stainless-steel autoclave at 120 °C for 8 h, following that the suspensions were dried at 140 °C for 48h. Eventually, the dried structures were pyrolyzed at 850 °C for 3 h.

Table 1. All samples and synthesis conditions

Sample	Grinding mode	Doped element/dopant	Solvent
PAS	grind	-	-
BPAS	ball-milling	-	-
S-BPAS	ball-milling	S/sulfur	cyclohexane
P-BPAS	ball-milling	P/red phosphorus	NMP
N-BPAS	ball-milling	N/melamine	glycerol

2. 3. Manufacturing the cement composites

The cement paste was first prepared with a water/cement mass ratio = 40% (v/w). Next, the pyrolyzed structures including grinded almond shell, ball-milled almond shell, sulfur-doped ball-milled almond shell, phosphorous-doped ball-milled almond shell, and nitrogen-doped ball-milled almond shell (abbreviated as PAS,

BPAS, S-BPAS, P-BPAS, and N-BPAS) were blended into the prepared dough in a low mass fraction of 10 wt% (guest/host+guest= 10%). Finally, the colloidal structures were molded at ambient temperature into rectangular shapes to investigate microwave-absorbing performance at x- and ku-band frequencies as well as energy-saving. A schematic illustration describing the synthetic routes is presented in Fig. 1.

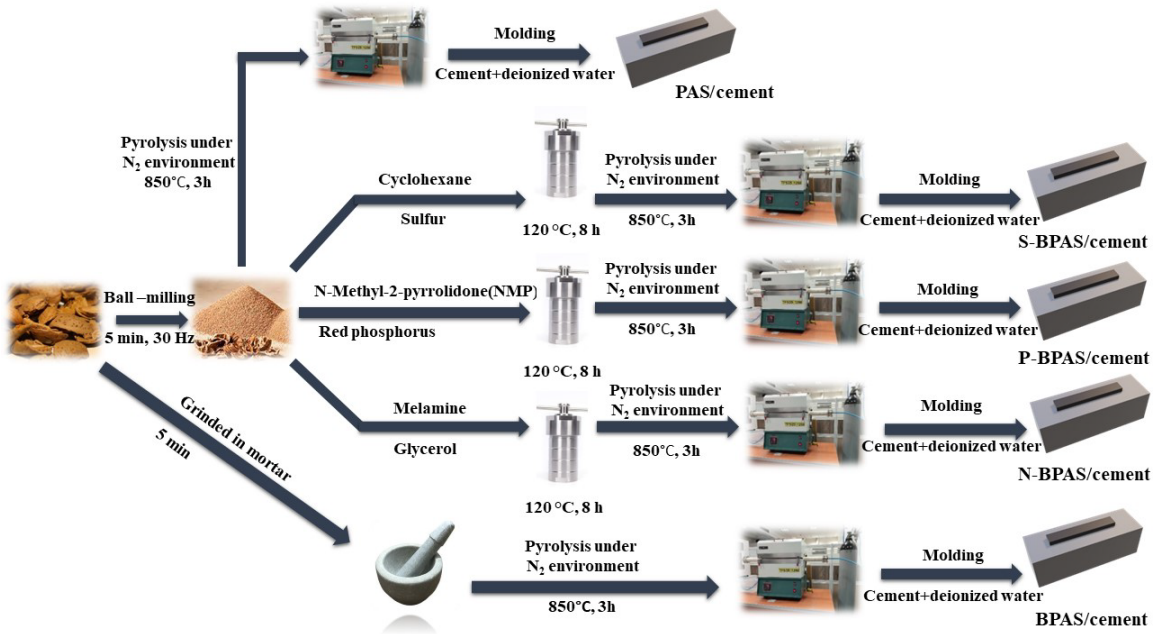


Fig. 1. Schematic illustration of the synthetic processes

2. 4.Characterization

ShimadzuMPC-2200 and8400 instruments recorded diffuse reflection spectroscopy (DRS) and Fourier transform infrared (FTIR) spectra meanwhile the X-ray powder diffraction (XRD) patterns, quantitative elemental analysis, and morphologies were revealed by D8 advance X-ray diffractometer from Bruker and Tescan Mira3 field

emission scanning electron microscopy (FE-SEM) combined with an energy dispersive spectroscopy (EDS), respectively. High-resolution transmission electron microscopy (HRTEM) results were examined by FEI TEC9G20. Surface characteristics were studied by N₂ adsorption/desorption results based on Brunauer-Emmett-Teller (BET) and Barrett-Joyner-Halenda (BJH) methods. A TAKRAM SRM Raman microscope fabricated in Teksan Co. operating at an excitation wavelength of 532 nm evaluated the doping, defect, and hybridization of the biomass-derived structures. The thermal resistance of the AS was evaluated by Perkin Elmer thermogravimetric analysis (TGA), while IR absorption of the samples was monitored by a FLIR ONE Pro thermal camera combined with an iPhone 9 for imaging. The milling procedure was done by a NARYA - MPM 4*250 ball-mill fabricated by Amin Asia. In the final step, microwave-absorbing/shielding characteristics of the samples molded by cement paste were clarified by an Agilent technology (E8364A) vector network analyzer operating by a waveguide technique at x- and ku-bands.

3. Results and discussions

3. 1. Structural and morphological characterization

Fig. 2 exposes the FTIR spectra, XRD patterns, TGA plot, Raman spectra, and the curves related to the surface features of the biomass-derived structures. The absorption bands assigned at 2919, 2843, 879, and 629 cm⁻¹ are associated with the

symmetric and asymmetric as well as in-plane and out-of-plane bending vibrations of C-H species meanwhile the broadband around 3400 and the notches observed at 1463 and 1380 cm^{-1} could be arisen by the stretching and deformation vibrations of hydroxyl functional groups ⁴¹⁻⁴³. As indicated, the alkene, alkoxy, and epoxy groups existed in BPAS, testified by the assigned peaks at 1627, 1106, and 1051 cm^{-1} ^{44, 45}. Notably, the denoted bump at 2357 cm^{-1} is ascribed to the adsorbed CO_2 . It can be seen that by sulphur doping, the hill around 529 cm^{-1} is widened, referring to the self-polymerization of the sulphur and doped olefin, bringing the overlapped peaks attributed to the C-S, S-S, and C-H bending vibrations. Furthermore, the thiol functional group was identified by the assigned shoulder around 2575 cm^{-1} ⁴⁶⁻⁴⁸. Interestingly, olefination was done to synthesis the carbon nanotube, catalyzed by phosphorus in the presence of the carbon feed supplied from the solvent and biomass. **The observed absorption band at 1737 cm^{-1} corresponds to the stretching vibrations of the carbonyl groups existing in the biomass-derived structure.** The reductive characteristics of red phosphorous and the olefination scenario weaken and shift the C=O absorption band to the higher wavelength ⁴⁹⁻⁵¹. **The peaks overlapped at 879 cm^{-1} and assigned at 1181 cm^{-1} are associated with the P-O-C and P-O vibrations, stemming from the coupled phosphorous** ⁵²⁻⁵⁵. The N-BPAS spectrum states that by nucleophilic attack of the amine-containing precursor, the epoxy rings were opened, confirmed by the

eliminated bump of epoxy group. Furthermore, the electrophilic active sites supplied by the carbonyl and carboxyl groups develop imine and amide groups after the condensation reactions under the pyrolysis process. Nonetheless, the bands related to the coupled and existing N-H, C-N, and C=N functional groups overlapped with the base peaks of the pyrolyzed structure^{56, 57}. More significantly, due to the lower electronegativity of P, S, and N elements compared to O, the redshift occurred for the absorption band at 1737 cm^{-1} ^{58, 59} (Fig. 2a). The presence of doping elements in the biomass-derived structures was confirmed by EDS results.

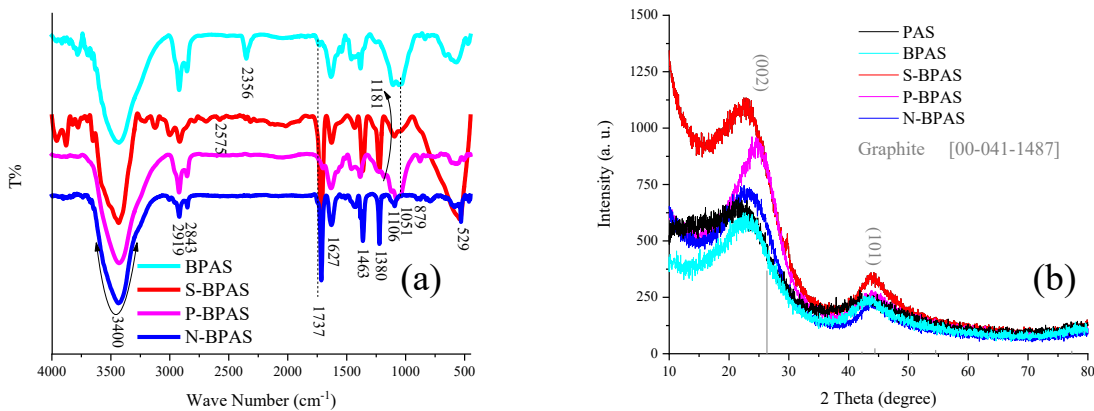
The XRD patterns are clarifying that the amorphous hexagonal crystal system was tailored after the pyrolysis process. The wide peaks around $2\theta=25^\circ$ and 42° imply the amorphous graphite, testified by JCPDS#: [00-041-1487] (Fig. 2b)⁴⁷. However, by exhausting the CO, CO₂, and other volatile structures after pyrolysis, the synthesized two-dimensional conjugated carbon-based layers have been expanded compared to the standard d-spacing of graphite layers (d-spacing = 3.37 Å). Note that the catalytic characteristics of phosphorous and olefination diminished the interlayer spacing and boosted the crystallinity of the biomass-derived structure, the decrease of I value in Raman spectra after pyrolysis is a strong proof⁶⁰ (Fig. 2c). Particularly, the crystal structure of graphite was maintained after the doping procedures. More specifically, the broad diffraction

peak at lower angles associated with the SBPAS could be attributed to the *in-situ* polymerization of sulphure as a doping agent, bringing polysulphide derivates.

It could be expected that after the ball-milling scenario, the intensity ratio of the D and G bands (I_D/I_G ratio) diminished originating from the decomposing of the carbon skeleton owing to the supplied activation energy, developing SP^3 hybridization and defects, desirable for polarization loss (Fig. 2c). It should be noted that N-, S-, and P-doping deteriorated SP^3 hybridization due to the catalytic feature of red P, implanting CNTs, graphite-like carbon nitride ($g-C_3N_4$) fabricated *in-situ*, and-derivates of sulphide polymers, treating the defected structures and developing SP_2 -based products. The thermal resistance of the AS was examined in a N_2 environment from 25 to 950 °C at a heating rate of 20 °C/min. Obviously, the adsorbed moisture evaporated at a temperature below 150 °C^{61, 62} meanwhile exhausting the oxygen-containing functional groups like CO_2 , CO, and other organic derivates as well as volatile species started from 250 °C and existed up to 400 °C (Fig.d).

The N_2 adsorption/desorption results are in good agreement with the other analyzes like SEM, Raman, and microwave characteristics. The surface parameters, including specific surface area (S_{BET}) and pore characteristics are summarized in Table S1. The achieved results manifest that through the milling process; the pore volume and S_{BET} were ameliorated, confirmed by the FESEM micrographs (Fig. b₁-

and c_{1-5}). This phenomenon broadened S_{BET} and was a great leap forward in developing a comparable prospect for producing practical and affordable structures, conventionally applying CNT and graphene^{63, 64}. Noteworthy, the surface characteristics are tunable by doping. The insertion of S boosted the S_{BET} and pore volume meanwhile BJH method suggested that the pore volume and S_{BET} were reduced by loading P and N dopants. The reason behind the observed phenomena can be interpreted by the derivatives synthesized after the pyrolysis procedure. Evidently, the g- C_3N_4 and CNTs formed *in-situ* decreased specific surface area and pore volume; nonetheless, the sulfidation augmented the surface characteristics. It should be noted that the specific surface area is the crucial parameter modulating microwave absorption, deduced from the Debye relaxation theory.



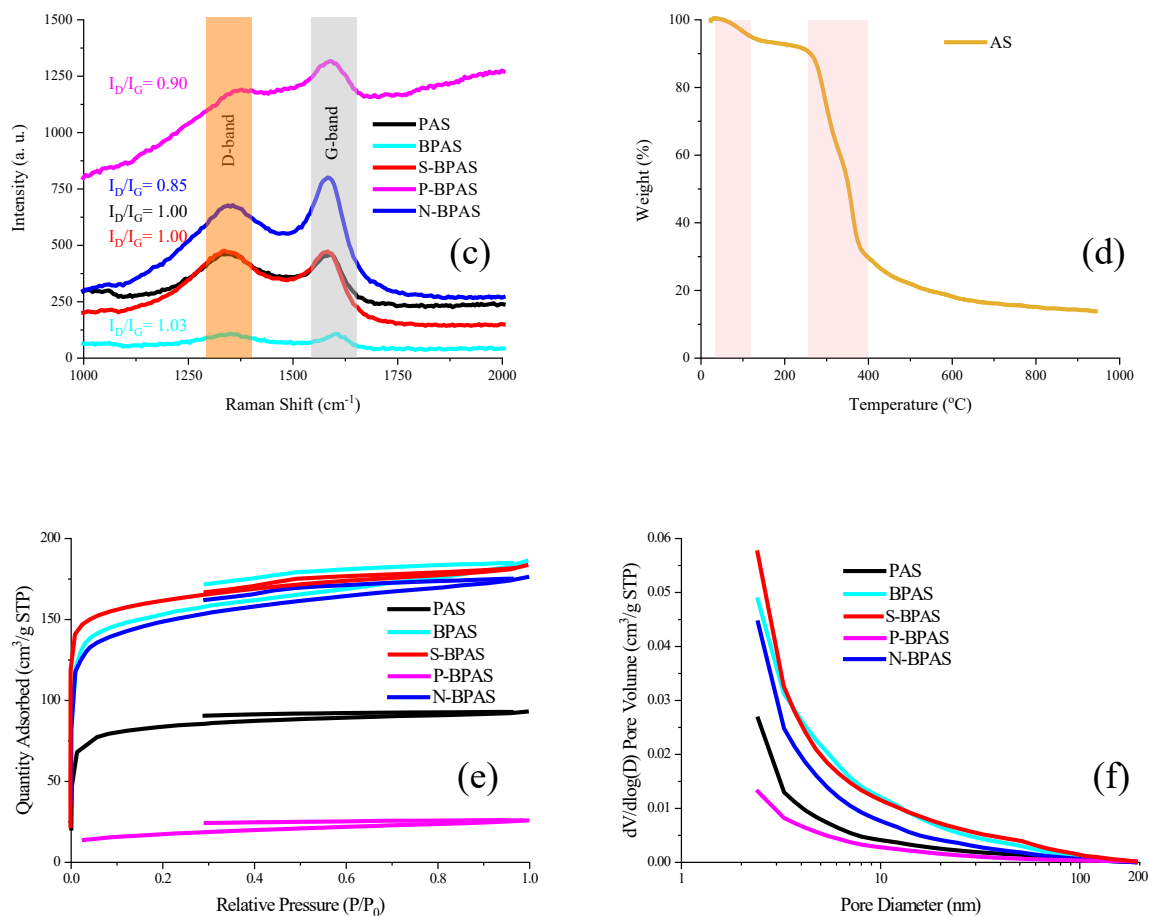


Fig. 2. FTIR spectra (a), XRD patterns (b), Raman spectra (c), TGA plot (d), N₂ adsorption/desorption isotherms (e) and pore size distributions (f) of the samples

FESEM of the samples with diverse magnifications has been shown in Fig. 3. As indicated, a uniform macroporous morphology of AS is detected with an average diameter of 1 μm , maintained after pyrolysis and ball-milling. Nevertheless, the obtained results refer that the average size of the biomass-derived material was reduced after the milling process. Evidently, by doping and depositing the product derived from the inserted elements, the porosity of the BPAS was diminished, as

testified by BET and BJH results. It is interesting to note that thanks to the insertion of red phosphorus, due to its catalytic ability in the presence of the carbon source, the CNTs were implanted with a diameter range from 20 to 70 nm. The quantitative results estimated by EDS analysis have been exposed in Fig 3, S1, and Table S2. The atomic and weight percentages (A% and W%) clearly declare that the doping scenario went well and led to an enhancement of the doped element in the eventual product. The achieved results manifest that the N content in the P-BPAS sample is the highest among all samples, with N=12.39%. However, the elemental content of N in N-PBAS is about N=4.09%. Two hypotheses are predictable for the observed phenomenon. On the one hand, the catalytic performance of the red phosphorous facilitates the exhaustion of the oxygen and carbon-containing functional groups from the biomass to implant CNTs, diminishing the mentioned elements fraction compared to the N, on the other hand, the electrostatic interactions between the NMP and the biomass, developing the covalent couplings after the heat treatments, augment the N-containing functional groups. The bulk structure of the P-BPAS observed in SEM micrographs as well as its diminished SBET confirm the deposited NMP onto the interface of the biomass-derived structure, acting as a feed to provide carbonaceous content for growth of the CNTs. Fig. 4 exposes the TEM and HRTEM images associated with the P-BPAS. The TEM results have parallelly testified to the growth of the CNTs in the

biowaste. The carbon feed was supplied by the bioinspired structure, while the catalytic performance was made by red phosphorous. The assigned Bragg diffractions ascribed to amorphous graphite observed in the XRD pattern were completely confirmed by the lattice fringe analysis and selected area electron diffraction (SAED) pattern. The SEM and TEM images testified the implanted CNTs into the biomass (clarified by yellow arrows in Figs. 3 and 4), originating from the catalytic performance of the red phosphorous beside the pyrolysis treatments using the carbon feeds supplied by the biomass and NMP. However, the morphology and amount of the CNTs can be modified by optimizing the amount of the carbon feeds and red phosphorous and the pyrolysis strategy.

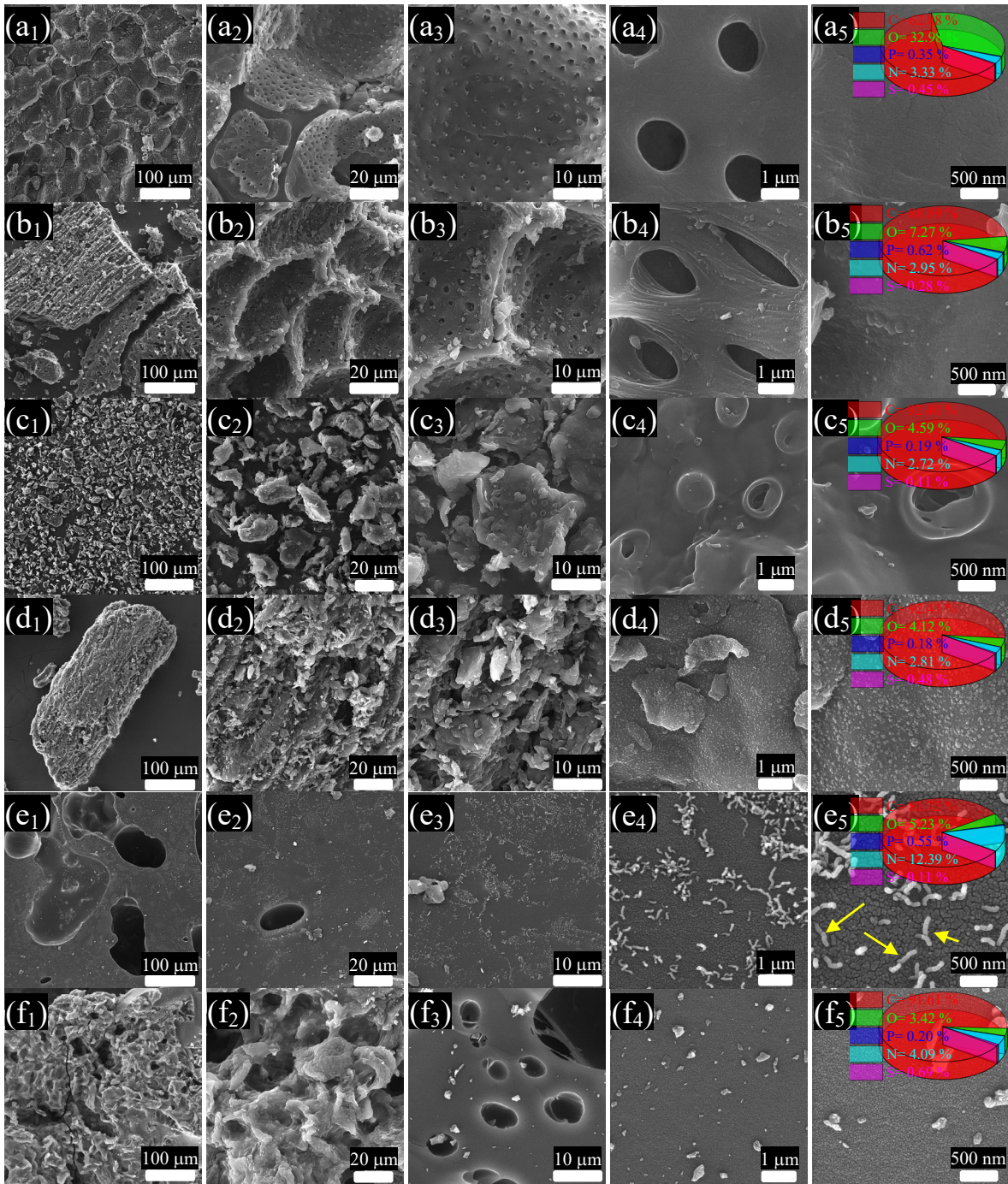


Fig. 3. FESEM micrographs (AS (a₁₋₅), PAS (b₁₋₅), BPAS (c₁₋₅), S-BPAS (d₁₋₅), P-BPAS (e₁₋₅), and N-PAS (f₁₋₅)) as well as A% (inserted pie chart)

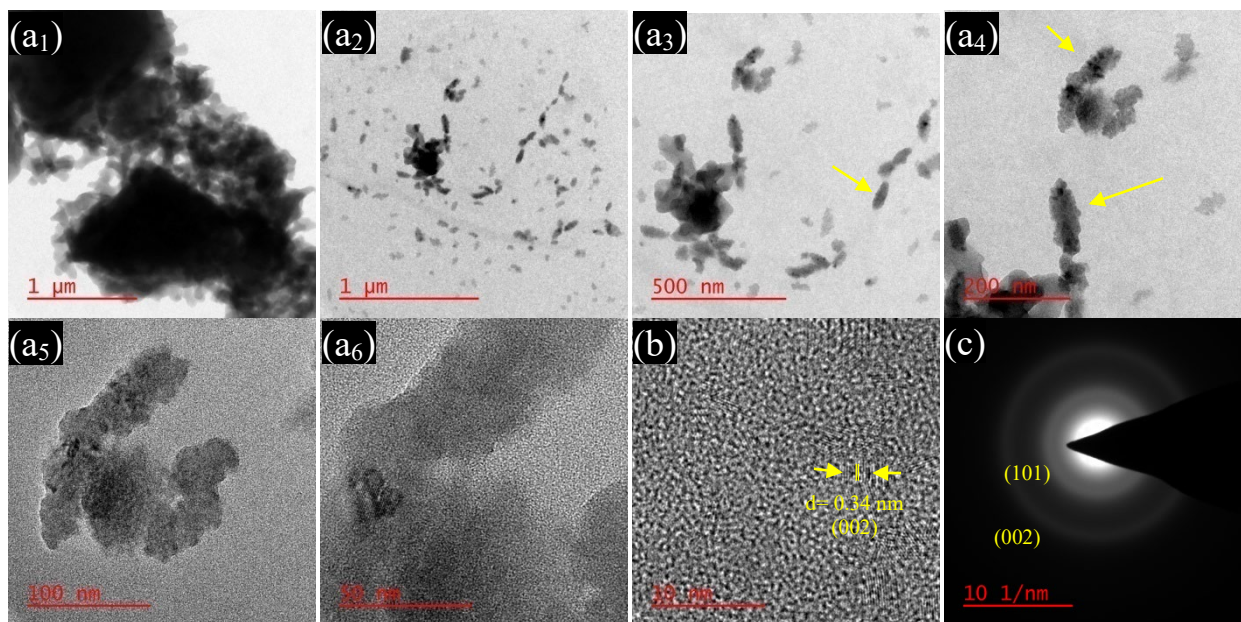


Fig. 4. TEM images (a₁₋₆), lattice fringe analysis (b), and SAED pattern (c) of P-BPAS

3. 2. Optical features and IR absorption

The UV-Vis absorption and monitoring of the IR absorption of the pyrolyzed samples are depicted in Fig. 5 and 6. The achieved curves imply that the doping phenomena have declined the absorption intensity of visible light. More importantly, the P-BPAS has shown the lowest results, generated from its lowest porosity, as confirmed by the BET and BJH results. However, the doping process has tuned the energy band gap (E_g) of the pyrolyzed biomass (Fig. 5b). The minimum energy needed to charge transition from the highest occupied molecular orbital (HOMO) to the lowest unoccupied molecular orbital (LUMO), defines the E_g , supplied by the irradiated photon. The Kubelka–Munk theory estimates the E_g

by the equations as follows: $(\alpha h \nu)^2 = h \nu - E_g$, $\alpha = -1/t \ln T$ and $T = 10^{-A}$, where T, h, A, α , ν , and t imply the transmittance, Planck constant, absorbance, absorption coefficient, frequency, and thickness, respectively. As revealed, the established functional groups as polarization centers by the doping process decreased the E_g . The lower band gap related to the P-BPAS attests to its polarizability potential, improving the relaxation loss in the microwave region and building a bridge between quantum and classical physics.

Global warming could be controlled by IR reflection/absorption, mitigating the outgoing and incoming heat by irradiations from buildings in diverse seasons. The huge proportion of received sunlight is placed in the IR region. The pyrolyzed biowastes were molded with cement to evaluate their performance in the IR region for practical applications. The temperatures of the samples were measured by an IR camera after 00:30, 01:00, 02:30, 05:00, 10:00, 15:00, 20:00, 40:00, and 60:00 minutes under an IR illuminator, arranged in rows according to the samples title list appeared in Fig. 6 (b). The obtained results illustrated that the doping procedure, synthesizing novel functional groups and boosting the diversity of bond vibrations as well as manipulated size, developing quasi-antenna, metamaterial, and plasmonic effect, are the key parameters regulating the IR absorption. Interestingly, the size modification by the milling route sacrifices the IR absorption. The reason for this adventure could come from the amplified quasi-

antenna, metamaterial, and plasmonic effect. Nevertheless, the doping scenario elevated IR absorption, rooted in the formed functional groups and bond vibrations. The presented prospect enhances the applications of building materials for energy-saving and microwave absorption.

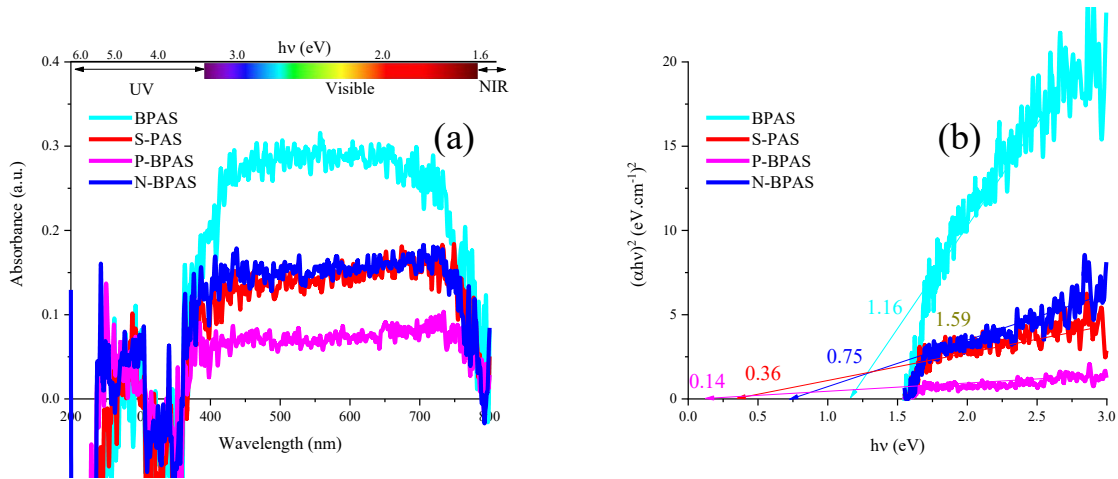


Fig. 5. Optical performance including the light absorption from 200 to 800 nm (a) and energy band gaps (b) of the samples

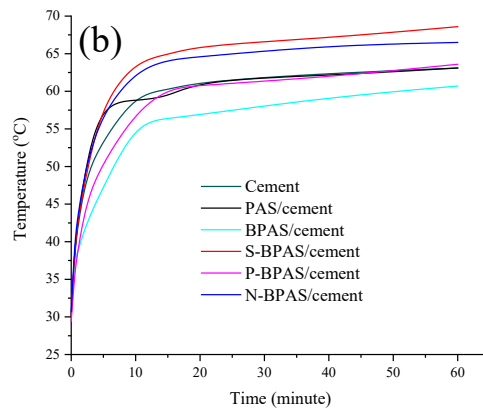
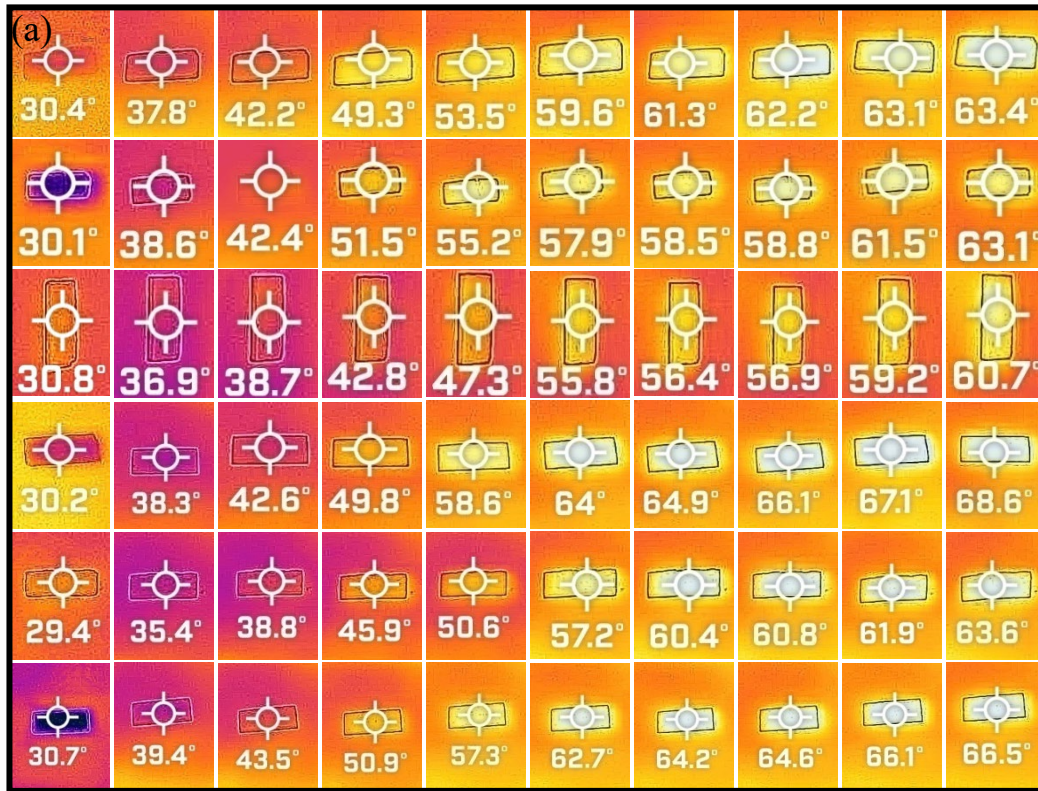
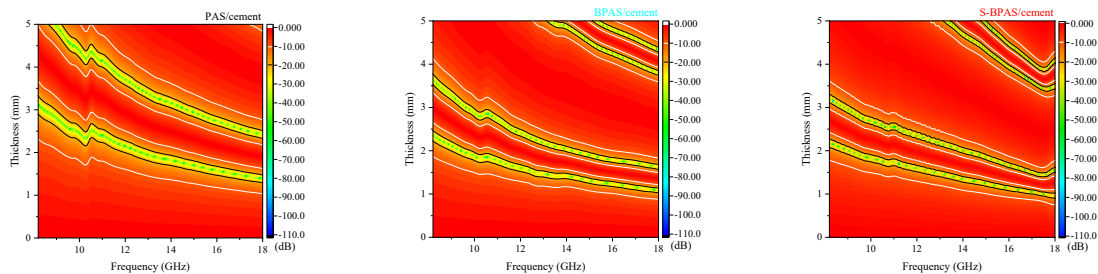


Fig. 6. Thermal images (a) and their derived chart (b) of the samples

3. 3. Microwave absorbing performance

The reflection loss (RL) *versus* frequency of the bio-inspired composites as well as the matching thickness associated with the efficient bandwidth ($RL \leq 10$ dB) and maximum RL of the samples were exposed in Figs. 7, S2, and 8. The reflection loss

was estimated by the transmission line theory based on the permittivity and permeability of a microwave absorber^{65, 66}. PAS/cement composite brought a RL value of -56.23 dB at 15.37 GHz and abroad efficient bandwidth (RL \leq -10 dB) of 6.06 GHz with only a thickness of 1.65 mm meanwhile S-BPAS/cement composite gained a fascinating RL of -99.42 dB at 8.33 GHz and efficient bandwidth (RL \leq -10 dB) as wide as 1.09 GHz with 3.15 mm thickness. The shifted maximum RL by changing the thickness is expressed by the quarter-wavelength mechanism, defined by the canceled reversal waves from the reflector that the absorber is placed on by the propagating waves from the threshold of the absorber when they are 180° out of phase and the thickness is an odd numeral of $\lambda/4$ of penetrated wave (Fig S2). Obviously, the quarter-wavelength mechanism is the pioneer mechanism consuming the input waves tunable by the permittivity and permeability of a filler^{67, 68}.



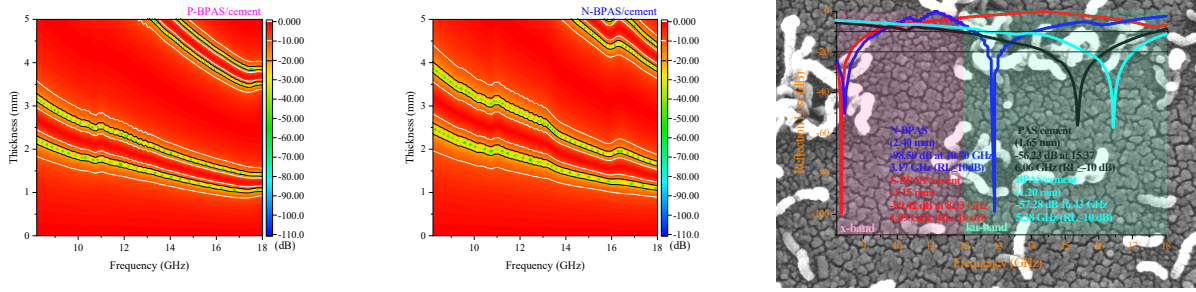


Fig. 7. Microwave absorption of the biomass-derived materials

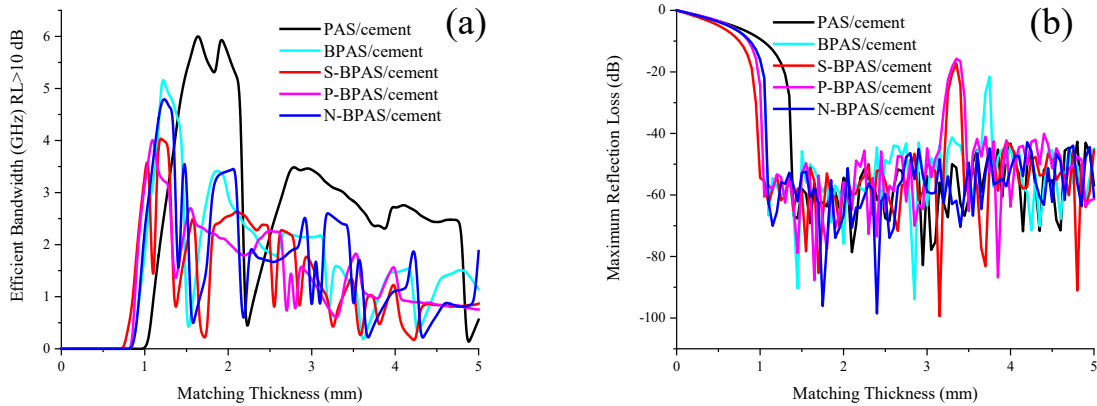


Fig. 8. Matching thickness related to the efficient bandwidth ($RL \leq 10$ dB) (a) and maximum RL (b) of the samples

The real and imaginary parts are dedicated to the storage and attenuation of the incident waves. The real and imaginary parts of the permittivity and permeability, Cole-Cole plot, impedance matching (Z), attenuation constant (α), alternating conductivity (σ_{AC}), eddy current (C_0), and skin depth (δ) are shown in Fig. 9. Real part of permittivity (ϵ') is essentially regulated by the dipole and interfacial polarization. It is worth noting that the milling process, by enhancing the

heterogeneous interfaces, as testified by the S_{BET} , elevated the polarization mechanism. Generally, the doped elements act as polarization centers, boosting the dipole polarization. Notably, the ϵ' curve of P-BPAS is in contract with S_{BET} results. The catalytic performance of red phosphorous, implanting CNTs, in the porous structure alleviates the space charge polarization meanwhile this performance augments the rough surface, desirable for the quasi-antenna polarization (Fig. 9a). The winner of the competition is the morphology and quasi-antenna capacity. The imaginary part of permittivity (ϵ'') mainly originates from the relaxation and conductive loss. It is well known that the reductive scenario under the inert gas and high temperature (pyrolysis) by exhausting the oxygen-containing functional groups, enhances the conjugated structures, as attested that by TGA and EDS analyses. The crucial parameter behind the electric conductivity of pyrolyzed carbon-based materials is π and n to π^* charge transitions. The non-bonding electrons of the hetero atoms that exist there after the reductive route provide n to π^* transitions⁶⁹. The achieved spectra declare that through the milling process, the relaxation and conductive loss were enhanced, stemming from the facilitated exhaust of the hetero atoms owing to the more heterogeneous interfaces (Fig. 9b). Alternating conductivity (σ_{AC}) curves scrupulously dissect the charge transition potential of the biomass-derived materials. Nevertheless, the broadened S_{BET} amplifies the relaxation loss mechanism⁷⁰⁻⁷². More significantly, doping the hetero

atoms based on their electronegativity deteriorated the conductive loss; nonetheless, they amplified the dipole polarization (Fig. 9h). The permeability is generated by the natural and exchange resonance as well as eddy current loss (C_0). The resonances could be established by the radicals created during pyrolysis. The parallel resonance peaks were observed around 10 GHz in real (μ') and imaginary (μ'') parts of permeability which could be derived from the charge circuits around the ordered hierarchical structure and established quasi-antenna feature (Fig. 9c-d), creating secondary fields and metamaterial property, interpreted by Oersted's and Lenz's law^{24, 31, 34, 73-80}. It should be noted that the destructive treatment by milling procedure diminished the holes and secondary fields, clarified by the reduced intensity of the notches. The types and intensity of polarization were investigated by drawing the Cole-Cole plot, governed by the Debye relaxation theory⁸¹⁻⁸⁴ (Fig. 9e). It is notable that the size and morphology pave the way for relaxation loss and the doping scenario augments the relaxation loss capacity. The more constant C_0 curve is in the trade-off between the more eddy current loss. Noticeably, by milling the bio-inspired structure, the eddy current loss was mitigated meanwhile the PAS demonstrated eddy current loss after 11.5 GHz (Fig. 9i). The synthesized functional groups by increasing the dipole polarizations alleviated the eddy current effect. Impedance matching (Z) and skin depth (δ) are the vital factors illustrating the propagation of incident microwaves inside the absorbing medium. The more

closing Z to 1 declares the more penetration of the input waves into the absorbing matrix, validated by the skin depth results⁸⁵⁻⁸⁷ (Fig. 9f, j). As the permeability and permittivity of an absorber are synchronized, the more impedance matching and skin depth be gained. Attenuation constant (α) indicates the ability of a microwave absorber to consume the electromagnetic energy and its conversion into thermal energy (Fig. 9g). Obviously, PAS exhibited the worst result, while milling treatment and doping scenario promoted the energy conversion, desirable for architecting the shielding materials, operating based on the absorption. A constructive compromise between Z and α brings a brilliant RL⁸⁸⁻⁹⁰.

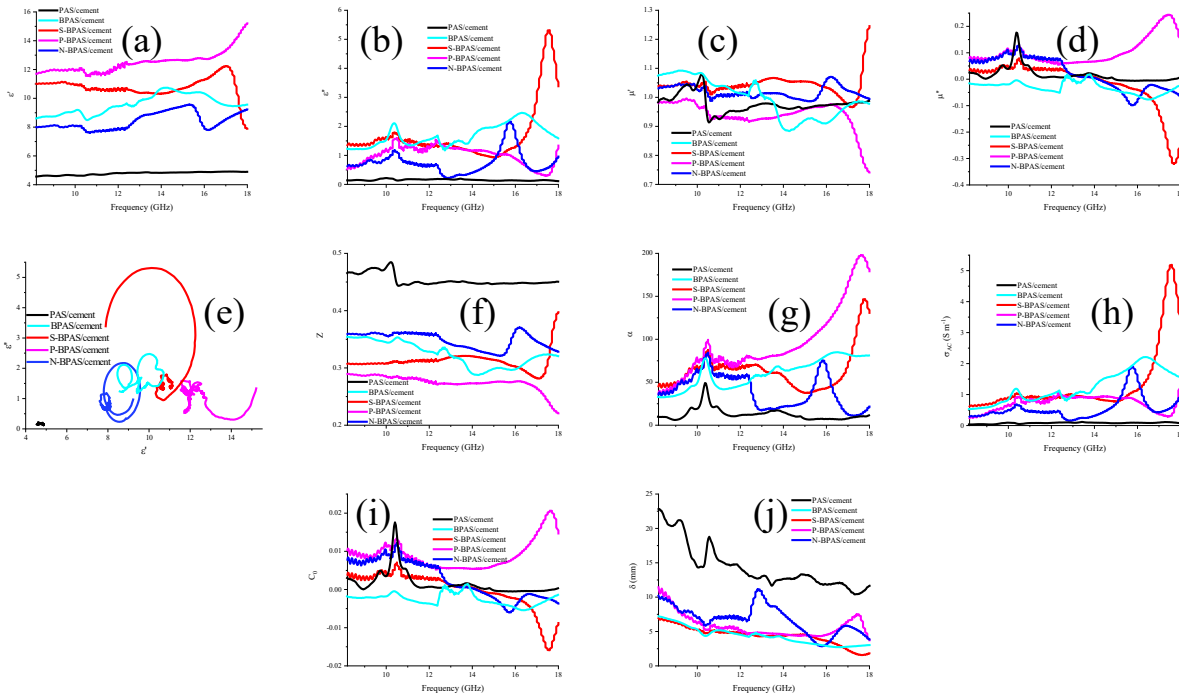
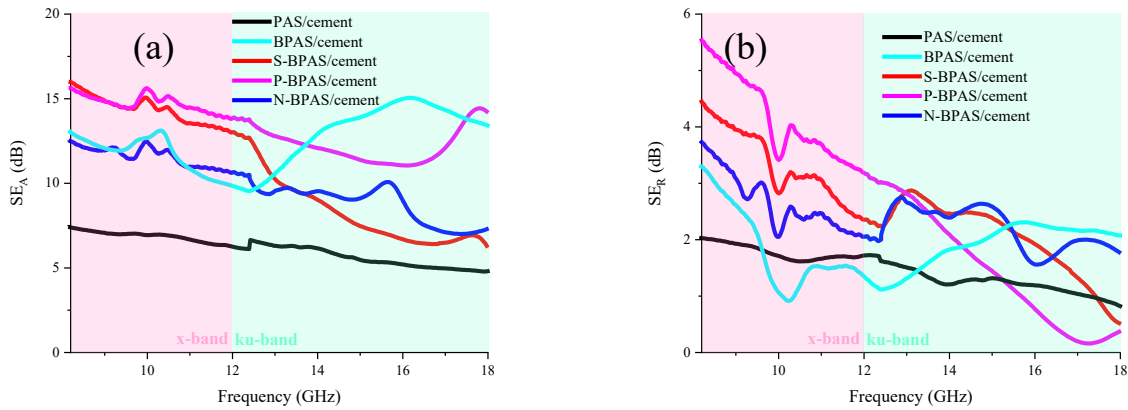


Fig. 9. ϵ' (a), ϵ'' (b), μ' (c), μ'' (d), Cole-Cole plot (e), Z (f), α (g), σ_{AC} (h), C_0 (i), and δ (j) *versus* frequency of the sample

The global concerns were excited by electromagnetic interference, the 4th pollutant of the environment, threatening any living species and ecosystems^{82, 91-96}. Hence, cement as a building material was strengthened by a cost-effective bio-waste to architect a microwave refiner. Primary shielding materials typically benefited from impedance mismatching, establishing secondary fields and pollution by reflecting the incident waves from their threshold. Gradually, electromagnetic shielding materials were tailored by regulating impedance matching and elevating absorbing properties. The sum of gained shielding effectiveness of absorbance (SE_A) and reflectance (SE_R) brings total shielding effectiveness (SE_T), exhibited in Fig. 10⁹⁷,⁹⁸. The sustainable and affordable biomass-derived material demonstrated the particular shielding absorption which can act as a microwave refiner in the polluted environments. Evidently, the size-modified biowaste and doped structures boost the SE_T , originating from the ameliorated conjugated carbon-based structure by pyrolysis, dipole polarization by doping scenario, interfacial polarization by milling and implanting the CNTs, as well as metamaterial features. Moreover, the impedance matching and multiple reflections and scattering pave the way for the achieved results. Particularly, BPAS and P-BPAS attained a total shielding effectiveness of more than 90% from 8.2 to 18 GHz. Due to the combined action of suitable impedance matching, dielectric loss and magnetic loss, the sample has excellent microwave absorption performance. The large specific surface area and

pore structure promote the formation of conductive network, optimize the impedance matching, and convert electromagnetic energy into heat energy. Specifically, 1) the pore structure will cause multiple reflections and scattering of incident electromagnetic waves; 2) The presence of oxygen-containing groups such as C-O and C=O in the composite material will form oxygen vacancies and oxygen defects, which will spontaneously form dipoles and polarization centers with P, N, S and other elements, resulting in polarization relaxation. In addition, the presence of pores increases the dipole moment and improves the EMA performance. **The absorption mechanism is the synergistic result of impedance matching and microwave attenuation capability**⁹⁹. All equations used to assess the microwave absorbing characteristics are tabulated in Tables S3 and S4.



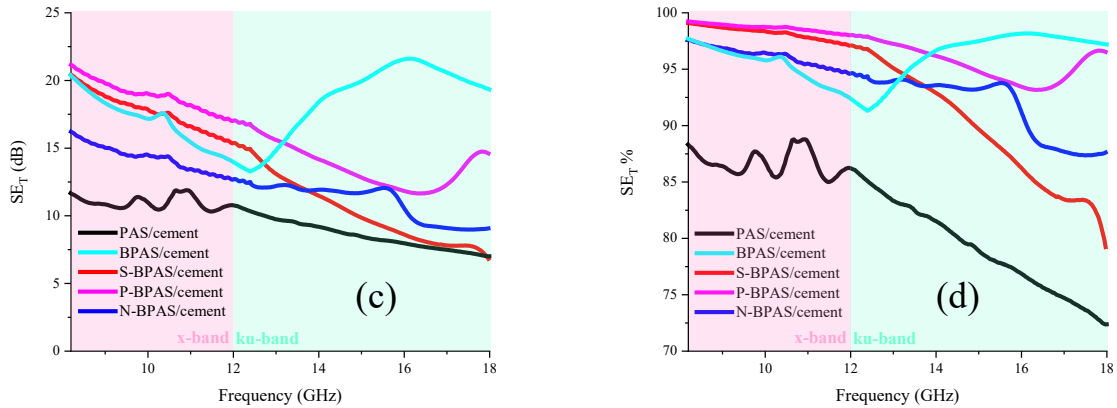


Fig. 10. SE_A (a), SE_R (b), SE_T (c), and percentage of SE_T (d) at x- and ku-band frequencies

3. 4. Electromagnetic wave absorbing mechanisms

Comparative results of microwave absorption performance relating to the reported biomass-derived structures are tabulated in Table 2. As indicated, the samples fabricated by almond shells demonstrated intense RL and broad efficient bandwidth with thin thickness compared to the other bio-waste-based microwave absorbers. The vast specific surface area of the almond shells due to their porosity, as testified by the SEM and BET results, plays the pioneer and crucial role in bringing microwave absorption. More interestingly, the ball milling process broadened the surface area to volume ratio, required for dipole and interfacial polarizations. On the other hand, the existing heteroatoms in the almond shell nature, as attested by EDS spectra, act as dipole polarization centers, favorable for microwave attenuation. Particularly, the dielectric performance and dipole

polarization were regulated by P, S, and N sources as doping agents. The doped elements by tuning the conductive loss and polarization capability modify the microwave absorbing ability of the samples. Specially, the red phosphorous implanted carbon nanotubes into the biomass as a carbon-based feed, ameliorating the microwave absorption. It is noteworthy that the various inorganic phases forming cement, as a microwave absorbing medium, improve the heterogeneous interfaces, deteriorating the propagated electromagnetic waves. It should be noted that the unpaired electrons, gained after pyrolysis, and the unique morphology of the precursor, establishing quasi-antenna and metamaterial features, promote permeability and impedance matching, desirable for electromagnetic wave absorption. The research presented two innovative faces. 1) The milling scenario by reducing the particle size and exhausting the oxygen-containing functional groups improved the maximum RL, matching thickness, and SE_T . S_{BET} and SEM results attested to the enhanced heterogeneous interfaces after the milling procedure meanwhile the Raman spectra testified the more defected structures and SP^3 -hybridized bonds. The broadened heterogeneous interfaces promoted the polarization-relaxation and conductive loss mechanisms, required for RL and shielding performance. The SE_T and the curves of the complex permittivity declared the claim. The milling treatment facilitated the exhaustion of oxygen-containing functional groups, which is desirable for defect and conductive loss, as

demonstrated by the EDS and permittivity results. 2) The elemental doping by the insertion of functional groups with electronegativity difference in the biomass-derived structure boosted the dipole polarizations and tuned the interfaces and defects, testified by the obtained polarization types and intensity (Fig. 9 (e)) as well as impedance matching (Fig. 9 (f)) diagrams. The deposition of the doping elements and their derived products diminished the S_{BET} although the unique morphologies from the milling process and the doping process ameliorated the metamaterials performance, favorable for establishing permeability and promoting impedance matching. The regulated doping strategies improved the biomass-derived structure's matching thickness, maximum RL, and SE_{T} . It should be noted that the quarter-wavelength is the pioneer and vital mechanism bringing RL of the cement-based samples, modulable by permittivity and permeability of the absorber. Fig. 11 shows an illustrative diagram of the significant mechanisms leading to microwave absorption.

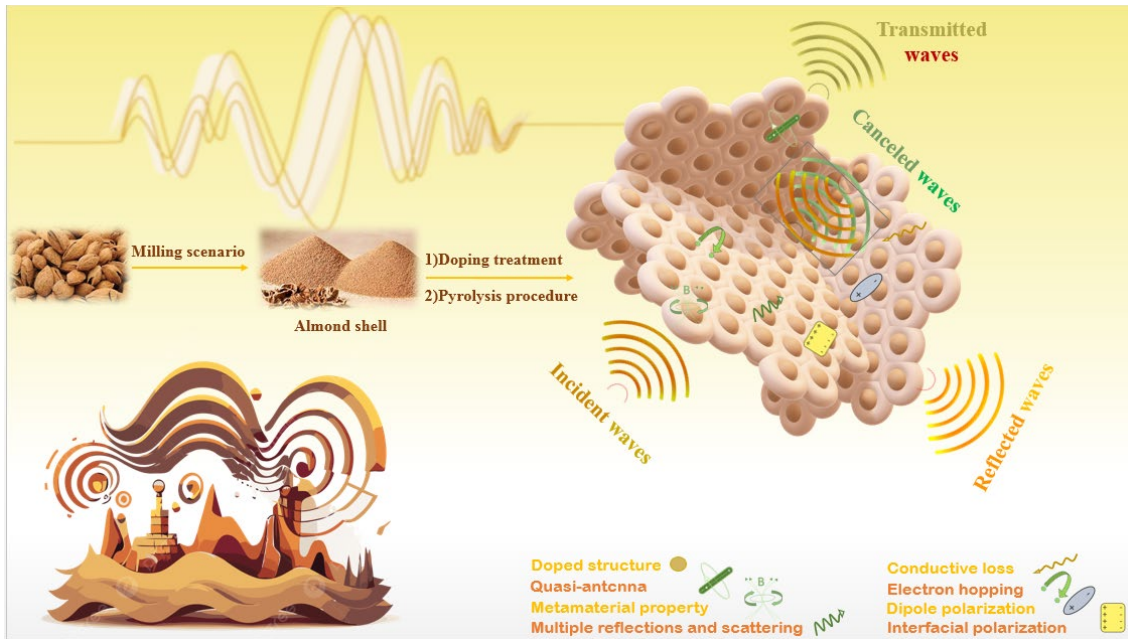


Fig. 11. An illustrative diagram of the significant mechanisms realizing the microwave absorption of the cement-based composites used as microwave absorbing refiner and energy-saving structure

Table 2. Comparative microwave absorption performance of the reported biomass-derived structures

Origin	Pyrolysis temperature (°C)	Promoting agent	Max. RL (dB)- Matching frequency (GHz)	Matching thickness (mm)	Efficient bandwidth RL<-10 dB (GHz)	Ref.
Populus euphratica	500	FCMT/CuCo ₂ S ₄ /PAN	-56.61-12.36	1.75	5.54	100
pine needle	800	porous morphology	-56.3-14.08	1.40	3.44	101
monarch butterfly wing scales	500	FCBW/ β -Co(OH) ₂ /PAN	-68.41-9.08	3.00	4.14	74

cellulose	800	nanofiber aerogel sphere morphology	-66.3-≈16.50	2.14	6.16	102
chitin	680	N-doped carbon aerogels	-68.80-10.05	5.10	4.20	103
Erodium cicutarium	500	FCMF/PAN	-49.47-14.19	2.00	8.13	75
lotus leaf	700	gradient Hierarchical Porous C/MoS ₂	-50.10-13.24	2.4	5.80	104
poplar catkin	550	sulfur-doped hollow carbon microtubes	-37.40-6.72	6.00	8.00	105
shaddock peel	800	aerogel morphology	-14.88-≈14.80	1.70	5.80	106
gelatin	800	Co/porous carbon framework	≈-32.00-≈14.10	2.30	6.60	107
fish skin	650	Foam morphology	-33.50-≈13.00	3.00	8.60	108
Platanus bark	800	Co@porous carbon	-49.20-10.00	3.22	6.16	109
corn cob	800	holey morphology	-47.00-14.10	1.90	5.50	110
grapefruit peel	700	CoFe ₂ O ₄ /carbon sheets/polyaniline	-51.81-12.40	2.57	7.20	111
chicken featherfiber	1400	doped porous carbon/epoxy	-20.10-10.20	2.00	2.90	112
almond shell	850	ball milling/porous morphology/cement	-57.28-16.43	1.20	5.38	this work
almond shell	850	N-doping/ball milling/porous morphology/cement	-98.50-10.70	2.40	3.17	this work

4. Conclusion

Climate change and electromagnetic pollution in the modern century, as a sleeping giant waiting to wake up, have augmented the global burden. The presented

platform endows a fascinating prospect for implanting CNT onto carbon-based materials, developing affordable precursors to facilitate and augment CNT-based applications. More interestingly, BPAS demonstrated an outstanding specific surface area, compared to graphene and CNT. Cement was regarded as a practical medium to fabricate microwave-absorbing and energy-saving building materials. Furthermore, the influence of size and doping factors were scrupulously dissected. The achieved results manifested that the doping and size of pyrolyzed almond shells regulate microwave-absorbing and energy-saving properties. The reason behind the observed phenomena is essentially stems from the conductivity of the conjugated structures, diverse polarizations, and metamaterial characteristics. The presented prospect sheds new light on the environmental refiner with advanced energy-saving applications. More interestingly, an innovative and affordable procedure was introduced to prepare CNTs.

Compliance with ethical standards

Conflict of interest: The authors have declared that have no conflict of interest in connection with this research.

References

1. S. Iijima and T. Ichihashi, *nature*, 1993, **363**, 603-605.
2. B. S. Harrison and A. Atala, *Biomaterials*, 2007, **28**, 344-353.
3. N. De Jonge and J. M. Bonard, *Philosophical Transactions of the Royal Society of London. Series A: Mathematical, Physical and Engineering Sciences*, 2004, **362**, 2239-2266.
4. P. M. Ajayan and O. Z. Zhou, *Carbon nanotubes: synthesis, structure, properties, and applications*, 2001, 391-425.

5. W. Hoenlein, F. Kreupl, G. S. Duesberg, A. P. Graham, M. Liebau, R. V. Seidel and E. Unger, *IEEE Transactions on components and packaging technologies*, 2004, **27**, 629-634.
6. M. F. De Volder, S. H. Tawfick, R. H. Baughman and A. J. Hart, *science*, 2013, **339**, 535-539.
7. L. Hu, D. S. Hecht and G. Gruner, *Chemical reviews*, 2010, **110**, 5790-5844.
8. N. Arora and N. Sharma, *Diamond and related materials*, 2014, **50**, 135-150.
9. Y.-L. Li, I. A. Kinloch and A. H. Windle, *Science*, 2004, **304**, 276-278.
10. A. Vornoli, L. Falcioni, D. Mandrioli, L. Bua and F. Belpoggi, *International journal of environmental research and public health*, 2019, **16**, 3379.
11. Y.-H. Hao, J. Zhang, H. Wang, H.-Y. Wang, J. Dong, X.-P. Xu, B.-W. Yao, L.-F. Wang, H.-M. Zhou and L. Zhao, *Scientific reports*, 2018, **8**, 1-9.
12. V. Garaj-Vrhovac, A. Fučić and D. Horvat, *Mutation Research Letters*, 1992, **281**, 181-186.
13. V. Garaj-Vrhovac, *Chemosphere*, 1999, **39**, 2301-2312.
14. M. E. Alkis, H. M. Bilgin, V. Akpolat, S. Dasdag, K. Yegin, M. C. Yavas and M. Z. Akdag, *Electromagnetic biology and medicine*, 2019, **38**, 32-47.
15. L. Zhao, Y. Sun, C. Yu, J. Chen, X. Xu, X. Zhang, H. Wang, J. Zhang, H. Wang and J. Dong, *Environmental Science and Pollution Research*, 2020, **27**, 40787-40794.
16. R. Peymanfar, E. Selseleh-Zakerin, A. Ahmadi, A. Saeidi and S. H. Tavassoli, *Scientific Reports*, 2021, **11**, 1-12.
17. Q. Li, J. Tan, Z. Wu, L. Wang, W. You, L. Wu and R. Che, *Carbon*, 2023, **201**, 150-160.
18. Z. Gao, A. Iqbal, T. Hassan, L. Zhang, H. Wu and C. M. Koo, *Advanced Science*, 2022, 2204151.
19. X. Huang, L. Zhang, G. Yu, J. Wei and G. Shao, *Journal of Materials Chemistry C*, 2023, **11**, 9804-9814.
20. R. Peymanfar and A. Mirkhan, *Chemical Engineering Journal*, 2022, DOI: <https://doi.org/10.1016/j.cej.2022.136903>, 136903.
21. Q. Wang, B. Niu, Y. Han, Q. Zheng, L. Li and M. Cao, *Chemical Engineering Journal*, 2023, **452**, 139042.
22. B. Yang, J. Fang, C. Xu, H. Cao, R. Zhang, B. Zhao, M. Huang, X. Wang, H. Lv and R. Che, *Nano-Micro Letters*, 2022, **14**, 1-13.
23. R. Peymanfar, H. Dogari, E. Selseleh-Zakerin, M. H. Hedayatzadeh, S. Daneshvar, N. Amiri-Ramsheh, H. Ghafuri, A. Mirkhan, G. Ji and B. Aslibeiki, *Frontiers in Materials*, 2023, **10**, 1133287.
24. R. Peymanfar, Z. S. Ershad, E. Selseleh-Zakerin and S. H. Tavassoli, *Ceramics International*, 2022, DOI: <https://doi.org/10.1016/j.ceramint.2022.03.314>.
25. H. Dogari, R. Peymanfar and H. Ghafuri, *RSC advances*, 2023, **13**, 22205-22215.
26. H. Zhang, J. Cheng, H. Wang, Z. Huang, Q. Zheng, G. Zheng, D. Zhang, R. Che and M. Cao, *Advanced Functional Materials*, 2022, **32**, 2108194.
27. Z. Wu, H. W. Cheng, C. Jin, B. Yang, C. Xu, K. Pei, H. Zhang, Z. Yang and R. Che, *Advanced Materials*, 2022, **34**, 2107538.
28. X. Guan, Z. Yang, Y. Zhu, L. Yang, M. Zhou, Y. Wu, L. Yang, T. Deng and G. Ji, *Carbon*, 2022, **188**, 1-11.
29. G. Chen, L. Zhang, B. Luo and H. Wu, *Journal of Colloid and Interface Science*, 2022, **607**, 24-33.
30. R. Peymanfar and F. Fazlalizadeh, *Chemical Engineering Journal*, 2020, **402**, 126089.
31. R. Peymanfar, E. Selseleh-Zakerin and A. Ahmadi, *Journal of Alloys and Compounds*, 2021, **867**, 159039.
32. L. Liang, W. Gu, Y. Wu, B. Zhang, G. Wang, Y. Yang and G. Ji, *Advanced Materials*, 2022, **34**, 2106195.
33. R. Peymanfar, S. Javanshir, M. R. Naimi-Jamal and S. H. Tavassoli, *Journal of Materials Science*, 2021, **56**, 17457-17477.
34. R. Peymanfar, M. Yektaei, S. Javanshir and E. Selseleh-Zakerin, *Polymer*, 2020, **209**, 122981.

35. B. Abu-Jdayil, A.-H. Mourad, W. Hittini, M. Hassan and S. Hameedi, *Construction and Building Materials*, 2019, **214**, 709-735.
36. C. Jia, C. Chen, R. Mi, T. Li, J. Dai, Z. Yang, Y. Pei, S. He, H. Bian and S.-H. Jang, *ACS nano*, 2019, **13**, 9993-10001.
37. R. Mi, C. Chen, T. Keplinger, Y. Pei, S. He, D. Liu, J. Li, J. Dai, E. Hitz and B. Yang, *Nature communications*, 2020, **11**, 3836.
38. X. Wang, T. Zhan, Y. Liu, J. Shi, B. Pan, Y. Zhang, L. Cai and S. Q. Shi, *ChemSusChem*, 2018, **11**, 4086-4093.
39. S. Lin, H. Wang, X. Zhang, D. Wang, D. Zu, J. Song, Z. Liu, Y. Huang, K. Huang and N. Tao, *Nano Energy*, 2019, **62**, 111-116.
40. X. Li, B. Sun, C. Sui, A. Nandi, H. Fang, Y. Peng, G. Tan and P.-C. Hsu, *Nature communications*, 2020, **11**, 6101.
41. R. Peymanfar and M. Rahmanisaghieh, *Materials Research Express*, 2018, **5**, 105012.
42. R. Peymanfar and M. Rahmanisaghieh, *Materials Research Express*, 2019, **6**, 105025.
43. R. Peymanfar and N. Khodamoradipoor, *physica status solidi (a)*, 2019, **216**, 1900057.
44. R. Peymanfar and F. Azadi, *Nano-Structures & Nano-Objects*, 2019, **17**, 112-122.
45. R. Peymanfar, S. Javanshir, M. R. Naimi-Jamal and A. Cheldavi, *Materials Research Express*, 2019, **6**, 075004.
46. R. Peymanfar, J. Karimi and R. Fallahi, *Journal of Applied Polymer Science*, 2020, **137**, 48430.
47. R. Peymanfar, S. Javanshir, M. R. Naimi-Jamal, A. Cheldavi and M. Esmkhani, *Journal of Electronic Materials*, 2019, **48**, 3086-3095.
48. S. S. S. Afghahi, R. Peymanfar, S. Javanshir, Y. Atassi and M. Jafarian, *Journal of Magnetism and Magnetic Materials*, 2017, **423**, 152-157.
49. R. Peymanfar, S. S. S. Afghahi and S. Javanshir, *Journal of nanoscience and nanotechnology*, 2019, **19**, 3911-3918.
50. E.-C. Cho, J.-H. Ciou, J.-H. Zheng, J. Pan, Y.-S. Hsiao, K.-C. Lee and J.-H. Huang, *Applied Surface Science*, 2015, **355**, 536-546.
51. J. Wang, Z. Li, S. Li, W. Qi, P. Liu, F. Liu, Y. Ye, L. Wu, L. Wang and W. Wu, *Plos one*, 2013, **8**, e72475.
52. T. Sai, S. Ran, Z. Guo, H. Yan, Y. Zhang, H. Wang, P. Song and Z. Fang, *Chemical Engineering Journal*, 2021, **409**, 128223.
53. J. Wang, B. Xu, X. Wang and Y. Liu, *Polymer Degradation and Stability*, 2021, **186**, 109516.
54. W. Zhang, Y. Leng, P. Zhao, J. Wang, D. Zhu and J. Huang, *Green chemistry*, 2011, **13**, 832-834.
55. J. Jiang, Y. Wang, Z. Luo, T. Qi, Y. Qiao, M. Zou and B. Wang, *Polymers*, 2019, **11**, 1155.
56. S. I. Cha, K. i. Miyazawa and J.-D. Kim, *Chemistry of Materials*, 2008, **20**, 1667-1669.
57. Q. Cai, Z. Hu, Q. Zhang, B. Li and Z. Shen, *Applied Surface Science*, 2017, **403**, 151-158.
58. K. Miyazawa, Y. Kuwasaki, A. Obayashi and M. Kuwabara, *Journal of Materials Research*, 2002, **17**, 83-88.
59. K.-A. Wang, A. Rao, P. Eklund, M. Dresselhaus and G. Dresselhaus, *Physical Review B*, 1993, **48**, 11375.
60. R. Peymanfar, A. Javidan and S. Javanshir, *Journal of Applied Polymer Science*, 2017, **134**, 45135.
61. Q. Jiang, M. Liu, C. Shao, X. Li, H. Liu, X. Li and Y. Liu, *Electrochimica Acta*, 2020, **330**, 135212.
62. X. He, F. Luzi, W. Yang, Z. Xiao, L. Torre, Y. Xie and D. Puglia, *ACS Sustainable Chemistry & Engineering*, 2018, **6**, 9966-9978.
63. A. Peigney, C. Laurent, E. Flahaut, R. Bacsa and A. Rousset, *Carbon*, 2001, **39**, 507-514.
64. M. Mehrli, E. Sadeghinezhad, M. A. Rosen, S. T. Latibari, M. Mehrli, H. S. C. Metselaar and S. N. Kazi, *Experimental thermal and fluid science*, 2015, **68**, 100-108.

65. H. Sun, Y. Zhang, Y. Wu, Y. Zhao, M. Zhou, L. Liu, S. Tang and G. Ji, *Journal of Materials Science & Technology*, 2022.
66. W. Zhang, E. Ding, W. Zhang, J. Li, C. Luo and L. Zhang, *Journal of Materials Chemistry C*, 2023, **11**, 9438-9448.
67. Y. Han, Q. Wang, Q. Zheng, M. Cao, J. Yuan and L. Li, *Materials Letters*, 2022, **325**, 132837.
68. L. Wang, M. Huang, X. Yu, W. You, B. Zhao, C. Liang, X. Liu, X. Zhang and R. Che, *Journal of Materials Science & Technology*, 2022, DOI: <https://doi.org/10.1016/j.jmst.2022.05.015>.
69. S. T. M. Tan, A. Giovannitti, A. Marks, M. Moser, T. J. Quill, I. McCulloch, A. Salleo and G. E. Bonacchini, *Advanced Materials*, 2022, **34**, 2202994.
70. D. Lan, H. Zhou and H. Wu, *Journal of Colloid and Interface Science*, 2023, **633**, 92-101.
71. J. Xu, C. Bian, J. Sun, D. Liu, X. Wang, Z. Xue, X. Meng and H. Wu, *Journal of Colloid and Interface Science*, 2023, **634**, 185-194.
72. J. Tao, L. Xu, C. Pei, Y. Gu, Y. He, X. Zhang, X. Tao, J. Zhou, Z. Yao and S. Tao, *Advanced Functional Materials*, 2022, 2211996.
73. S. Keykavous-Amand and R. Peymanfar, *Scientific Reports*, 2021, **11**, 1-13.
74. R. Peymanfar and S. Ghorbanian-Gezaforodi, *Nanotechnology*, 2021, **32**, 195201.
75. R. Peymanfar and F. Moradi, *Nanotechnology*, 2020, **32**, 065201.
76. R. Peymanfar and F. Fazlalizadeh, *Journal of Alloys and Compounds*, 2020, **854**, 157273.
77. R. Peymanfar, A. Mohammadi and S. Javanshir, *Composites Communications*, 2020, 100421.
78. R. Peymanfar, S. Keykavous-Amand, M. M. Abadi and Y. Yassi, *Construction and Building Materials*, 2020, **263**, 120042.
79. W. Li, M. Xu, H. X. Xu, X. Wang and W. Huang, *Advanced Materials*, 2022, 2202509.
80. L. Yao, S. Zhou, L. Pan, H. Mei, Y. Li, K. G. Dassios, P. Colombo, L. Cheng and L. Zhang, *Advanced Functional Materials*, 2022, 2209340.
81. D. Han, G. You, Y. Zhang, H. Tian, J. He, J. Liang, H. Wang, C.-A. Wang, R. Zhang and G. Shao, *Journal of Materials Chemistry C*, 2023, **11**, 6130-6137.
82. Z. Zhou, X. Yang, D. Zhang, H. Zhang, J. Cheng, Y. Xiong, Z. Huang, H. Wang, P. Zhang and G. Zheng, *Advanced Composites and Hybrid Materials*, 2022, 1-11.
83. X. Chen, Z. Wang, M. Zhou, Y. Zhao, S. Tang and G. Ji, *Chemical Engineering Journal*, 2023, **452**, 139110.
84. B. Zhao, Z. Yan, Y. Du, L. Rao, G. Chen, Y. Wu, L. Yang, J. Zhang, L. Wu and D. W. Zhang, *Advanced Materials*, 2023, 2210243.
85. B. Zhao, Y. Du, Z. Yan, L. Rao, G. Chen, M. Yuan, L. Yang, J. Zhang and R. Che, *Advanced Functional Materials*, 2022, 2209924.
86. W. Gu, S. J. H. Ong, Y. Shen, W. Guo, Y. Fang, G. Ji and Z. J. Xu, *Advanced Science*, 2022, **9**, 2204165.
87. L.-L. Han, W.-W. Wu, C. Yuan, Z. Wang, X.-B. Zhou, X.-M. Chen and P. Liu, *Journal of Materials Chemistry C*, 2023, **11**, 5534-5545.
88. J. Tao, L. Xu, H. Jin, Y. Gu, J. Zhou, Z. Yao, X. Tao, P. Chen, D. Wang and Z. Li, *Advanced Powder Materials*, 2023, **2**, 100091.
89. X. Zhao, D. Zhu, J. Wu, R. Zhang, X. Lu, B. Fan, Y. Li and H. Wu, *Composites Communications*, 2022, **35**, 101320.
90. Z. Zhao, L. Zhang and H. Wu, *Advanced Materials*, 2022, **34**, 2205376.
91. M. Huang, L. Wang, B. Zhao, G. Chen and R. Che, *Journal of Materials Science & Technology*, 2023, **138**, 149-156.
92. M. Zhou, J. Wang, S. Tan and G. Ji, *Materials Today Physics*, 2023, 100962.
93. L. Yao, W. Cao, J. Zhao, Q. Zheng, Y. Wang, S. Jiang, Q. Pan, J. Song, Y. Zhu and M. Cao, *Journal of Materials Science & Technology*, 2022, **127**, 48-60.

94. Y.-S. Fang, J. Yuan, T.-T. Liu, Q.-Q. Wang, W.-Q. Cao and M.-S. Cao, *Carbon*, 2022, DOI: <https://doi.org/10.1016/j.carbon.2022.09.043>.
95. Y. Xie, S. Liu, K. Huang, B. Chen, P. Shi, Z. Chen, B. Liu, K. Liu, Z. Wu and K. Chen, *Advanced Materials*, 2022, 2202982.
96. Z. Ma, L. Zhang, X. Wang, G. Xiao, Y. Feng, W. Wang, K. Tian, D. Liang, Y. Yao and Q. Li, *Journal of Materials Chemistry C*, 2023, **11**, 12057-12067.
97. H. Yu, L. Yu, X. Qi, J. Cui, K. Wu, Y. Liu, L. Chen and X. Li, *Journal of Materials Chemistry C*, 2023, **11**, 10455-10463.
98. X. Guo, Y. Liu, S. Yang, H. Jia, L. Gao, X. Tian, Z. Tao, J. Liu, X. Yan and Z. Liu, *Journal of Materials Chemistry C*, 2023, **11**, 13526-13538.
99. Z. Lu, Y. Zhang, H. Wang, C. Xia, Y. Liu, S. Dou, Y. Li and J. Tan, *Engineering*, 2022.
100. R. Peymanfar, E. Selseleh-Zakerin, A. Ahmadi and S. H. Tavassoli, *Scientific reports*, 2021, **11**, 11932.
101. R. Zhang, J. Qiao, X. Zhang, Y. Yang, S. Zheng, B. Li, W. Liu, J. Liu and Z. Zeng, *Materials Chemistry and Physics*, 2022, **289**, 126437.
102. R. Zhang, N. Wu, F. Pan, Y. Yang, B. Li, L. Wu, W. Liu, J. Liu and Z. Zeng, *Carbon*, 2023, **203**, 181-190.
103. Y. Tian, D. Estevez, H. Wei, M. Peng, L. Zhou, P. Xu, C. Wu, M. Yan, H. Wang and H.-X. Peng, *Chemical Engineering Journal*, 2021, **421**, 129781.
104. F. Pan, Z. Liu, B. Deng, Y. Dong, X. Zhu, C. Huang and W. Lu, *Nano-micro letters*, 2021, **13**, 1-17.
105. F. Huang, S. Wang, W. Ding, M. Zhang, X. Kong, Z. Sheng and Q. Liu, *Journal of Materials Science: Materials in Electronics*, 2021, **32**, 6260-6268.
106. W. Gu, J. Sheng, Q. Huang, G. Wang, J. Chen and G. Ji, *Nano-Micro Letters*, 2021, **13**, 1-14.
107. X. Lu, X. Li, W. Zhu and H. Xu, *Carbon*, 2022, **191**, 600-609.
108. X. Zhou, Z. Jia, A. Feng, X. Wang, J. Liu, M. Zhang, H. Cao and G. Wu, *Carbon*, 2019, **152**, 827-836.
109. J. Cui, X. Wang, L. Huang, C. Zhang, Y. Yuan and Y. Li, *Carbon*, 2022, **187**, 115-125.
110. S. Wang, Q. Li, K. Hu, S. Wang, Q. Liu and X. Kong, *Applied Surface Science*, 2021, **544**, 148891.
111. T. Hou, Z. Jia, A. Feng, Z. Zhou, X. Liu, H. Lv and G. Wu, *Journal of Materials Science & Technology*, 2021, **68**, 61-69.
112. S. K. Singh, H. Prakash, M. Akhtar and K. K. Kar, *ACS sustainable chemistry & engineering*, 2018, **6**, 5381-5393.